The Astrophysical Journal, 620:774–785, 2005 February 20

THE PROMINENT DUST EMISSION FEATURE NEAR 8.9 μm IN FOUR H II REGIONS

E. Peeters,[1,2] A. G. G. M. Tielens,[2] A. C. A. Boogert,[3] T. L. Hayward,[4] and L. J. Allamandola[1]

Received 2004 July 15; accepted 2004 October 29

ABSTRACT

We present a mid-infrared study of four H II regions based on the combination of *Infrared Space Observatory* (*ISO*) SWS observations with spatial information from SpectroCam-10 images and long-slit spectra. We report a prominent broad emission feature near 8.9 μm. The peak position and width of this feature do not resemble known polycyclic aromatic hydrocarbon (PAH) or dust emission features. Its spatial distribution is analyzed for two H II regions and is clearly distinct from that of the PAH emission features, being more similar to that of the ionized gas and especially to the spatial distribution of the dust continuum at 15 μm. Thus, the carrier of this band likely resides within the H II region. Possible carriers of this feature are highlighted.

Subject headings: H II regions — infrared: ISM — ISM: lines and bands — ISM: molecules

1. INTRODUCTION

The evolution of dust in regions of massive star formation is one key question in interstellar dust research. The distribution of dust in and around the ionized gas may well contain important clues to address this question. In particular, it has long been speculated that during the star formation process, dust infall is stopped by radiation pressure from the luminous protostar. Indeed, the wall of dust formed this way may stop or even reverse the infall motion of the gas as well (Larson & Starrfield 1971; Kahn 1974; Yorke 1986; Wolfire & Cassinelli 1987). This process has potentially important implications. It may control the maximum mass of stars formed (Larson & Starrfield 1971; Kahn 1974; Yorke 1986; Wolfire & Cassinelli 1987). It may also lead to deviating abundance patterns in massive stars (e.g., Mathis 1970). In addition, of course, it could lead to dust-free gas regions surrounding massive stars (Larson & Starrfield 1971; Kahn 1974; Yorke 1986; Wolfire & Cassinelli 1987). Furthermore, dust can also be destroyed in the ionized gas by physical or chemical sputtering (Barlow & Silk 1977; Draine & Salpeter 1979a, 1979b).

Infrared (IR) spectroscopy can provide direct information on the composition of interstellar dust and, in particular, probe the spatial distribution of the different dust components. The overall mid-IR (MIR) spectra of H II regions are dominated by a strong rising dust continuum and strong emission features at 3.3, 6.2, 7.7, 8.6, and 11.2 μm commonly called the unidentified infrared (UIR) bands. These UIR bands are generally attributed to emission by polycyclic aromatic hydrocarbon (PAH) molecules (Léger & Puget 1984; Allamandola et al. 1985, 1989; Puget & Léger 1989). Spectroscopy of a large sample of sources whose spectra are dominated by these UIR bands has now firmly established that the detailed characteristics of these bands vary from source to source and even within sources (Bregman 1989; Geballe et al. 1989; Joblin et al. 1996; Roelfsema et al. 1996; Verstraete et al. 1996; Maillard et al. 1999; Van Kerckhoven et al. 2000; Hony et al. 2001; Vermeij et al. 2002; Peeters et al. 2002b, 2004a, 2004b; Bregman & Temi 2005; Miyata et al. 2004; van Diedenhoven et al. 2004). These variations are likely due to physical modifications (e.g., charge state) and/or chemical modifications (e.g., loss of side groups or even destruction of some PAHs) of the interstellar PAH family reflecting local physical conditions. Studies of these variations have the potential to reveal much about the characteristics of the emitting PAH family and probe varying conditions within the emission zones.

Roelfsema et al. (1996) found that the source IRAS 18434−0242 has an extraordinarily strong 8.6 μm PAH band. In a study on the PAH band profiles, Peeters et al. (2002b) concluded that this band is clearly different from the "classical" 8.6 μm PAH emission feature. Similarly, Cesarsky et al. (1996) and Verstraete et al. (1996) found a broad, intense emission band at 8.7 μm in the H II region of M17, also clearly distinct from the 8.6 μm PAH band found in the PDR and molecular cloud of M17. Therefore, this emission band is a new and unique spectral characteristic of both sources, and further study is warranted to investigate its characteristics and, in particular, its relationship to the UIR bands.

In this paper we present an MIR study of the characteristics of this peculiar emission feature, based on *Infrared Space Observatory* (*ISO*) Short Wavelength Spectrometer (SWS) observations and slit spectra and images obtained with SpectroCam-10 (SC10). In § 2 we summarize the source characteristics. In § 3 we describe the observations and the data reduction. The feature profile is derived for all sources in § 4. Subsequently, the spatial variations of this band are analyzed in §§ 5 and 6. In § 7 the nature of this broad emission feature around 8.9 μm is highlighted and the implications of the spatial distribution of the different dust components are described. Finally, in § 8 we summarize our results.

2. SOURCE CHARACTERISTICS

Our sample consists of three compact H II regions and three positions within the giant H II region M17. Here we give an overview of the characteristics of each source.

2.1. *IRAS 18434−0242*

IRAS 18434−0242 (G29.96−0.02, hereafter IRAS 18434) is one of the best studied compact H II regions situated at

[1] NASA Ames Research Center, MS 245-6, Moffett Field, CA 94035; epeeters@mail.arc.nasa.gov.
[2] SRON National Institute for Space Research and Kapteyn Institute, P.O. Box 800, 9700 AV Groningen, Netherlands.
[3] California Institute of Technology, Division of Physics, Mathematics, and Astronomy, MS 105-24, Pasadena, CA 91125.
[4] Gemini Observatory, Southern Operations Center, Casilla 603, La Serena, Chile.

heliocentric distance of 5.7 kpc (Peeters et al. 2002a; $1'' = 0.028$ pc). This compact H II region is classified as cometary (Wood & Churchwell 1989). A young stellar cluster is embedded in the H II region, and the exciting star of IRAS 18434 is identified (Fey et al. 1995; Lumsden & Hoare 1996; Watson et al. 1997; Pratap et al. 1999) and has a spectral type of O6–O5 (Watson & Hanson 1997; Kaper et al. 2002a, 2002b).

The H II region is embedded in a molecular cloud (Churchwell et al. 1990, 1992). A hot core (HC) is located $\sim 2''$ west of the arc (Cesaroni et al. 1994, 1998; Hatchell et al. 1998; Pratap et al. 1999; Maxia et al. 2001; De Buizer et al. 2002). Detection of H_2O, H_2CO, and CH_3OH masers (Pratap et al. 1994; Hofner & Churchwell 1996; Walsh et al. 1998; Minier et al. 2000; Minier & Booth 2002), which are strongly associated with recent star formation, toward the HC and the $\sim 2''$ separation between the HC and the compact H II region indicate that the HC is not heated by the ionizing star of IRAS 18434 but rather harbors a massive protostar that has not yet ionized a compact H II region. This is supported by recent millimeter studies indicating the presence of an embedded outflow in the HC perpendicular to the direction of the H II region (Gibb et al. 2004).

2.2. *M17*

The H II region M17 is one of the closest and best studied regions of massive star formation, at a proximity of ~ 1.3 kpc (i.e., heliocentric distance, $1'' = 0.006$ pc; Hanson et al. 1997). Radio maps show two intersecting "bars," referred to as the N and S bars (e.g., Schraml & Mezger 1969; Lobert & Goss 1978; Felli et al. 1984). The N bar corresponds to the optically visible bar in M17 (Felli et al. 1984). The dense molecular cloud M17-SW is associated with the M17 H II region (Lada 1976) and externally heated by its exciting stars (Gatley et al. 1979). Various studies indicate that both the H II region and the molecular cloud are highly clumpy (Linke & Goldsmith 1980; Felli et al. 1984; Stutzki et al. 1988; Stutzki & Guesten 1990; Meixner et al. 1992; Burton et al. 1990, 2002). The southwest boundary of the S bar with this molecular cloud is an ionization front (I-front) viewed almost edge-on. Icke et al. (1980) estimated from modeling of the far-infrared (FIR) and radio continuum emission that the I-front makes an angle of 20° with the line of sight. A cluster of hot stars excites the H II region and triggers second-generation star formation in the nebular bars (e.g., Ogura & Ishida 1976; Chini et al. 1980; Hanson et al. 1997; Jiang et al. 2002). A total of 13 OB stars have been spectroscopically identified and estimated to be $\sim 10^6$ yr old (Hanson et al. 1997).

2.3. *IRAS 15567−5236*

IRAS 15567−5236 (G329.34+0.15, hereafter IRAS 15567) is classified as a cometary compact H II region based on radio continuum observations (Walsh et al. 1998). It is located at a near or far heliocentric distance of 7.8 or 9.6 kpc, respectively (Walsh et al. 1997). CH_3OH masers are detected and clearly associated with IRAS 15567 (Ellingsen et al. 1996; Walsh et al. 1998). It has also been detected at 1.2 mm (Pestalozzi et al. 2002). The spectral type of the ionizing star is estimated to be $\leq$O4 assuming that a single star produces the FIR radiation as observed by *IRAS* (Walsh et al. 1997).

2.4. *K3-50 A*

K3-50 A (IRAS 19598+3324) is a well-studied ultracompact H II region at a heliocentric distance of 8.2 kpc (Araya et al. 2002; Peeters et al. 2002a; Alvarez et al. 2004). It is classified as a compact radio shell by Turner & Matthews (1984) and as a core halo source by Kurtz et al. (1994). K3-50 A is the brightest and youngest of a complex of four radio sources (K3-50 A–D) at different stages of star formation, spread over an area of $3'.5$ (i.e., 8 pc). At optical wavelengths, K3-50 D is dominating while K3-50 A is coincident with a 10 μm peak (Wynn-Williams et al. 1977) and also with a CS core (Bronfman et al. 1996). Radio observations of K3-50 A suggest the presence of moving ionized material (e.g., Rubin & Turner 1969; Wink et al. 1983; Roelfsema et al. 1988; de Pree et al. 1994). In particular, de Pree et al. (1994) show that K3-50 A has a high-velocity bipolar outflow in the northwest-southeast direction. Based on CO observations, Phillips & Mampaso (1991) infer a molecular bipolar outflow viewed nearly pole-on. In contrast, Howard et al. (1996) suggest that the overall structure appears to be that of a rotating torus of dense gas with a bipolar ionized outflow. NIR observations suggest the existence of multiple ionizing stars (Howard et al. 1996; Okamoto et al. 2003; Hofmann et al. 2004; Alvarez et al. 2004), at least one with spectral types O7–O9 and two O9–B0 stars (Okamoto et al. 2003). Hofmann et al. (2004) and Alvarez et al. (2004) found up to 54 pointlike sources, some of them also rather massive.

3. OBSERVATIONS

3.1. *The ISO SWS Observations*

The three compact H II regions and the three positions within M17 were observed with SWS (de Graauw et al. 1996) on board *ISO* (Kessler et al. 1996). *ISO* SWS has observed 10 equally spaced positions in M17 along a $3'.5$ northeast-southwest cut, perpendicular to the I-front at the southwest boundary of the S bar (from R.A. $= 18^h17^m35^s.9$, decl. $= -16^\circ13'14''$ to R.A. $= 18^h17^m23^s.4$, decl. $= -16^\circ14'44''$, B1950.0 equinox), identical to that of Stutzki et al. (1988; see their Fig. 1 for position of the cut). The first three positions (used in this paper) are located in the H II region (S bar), positions 4–6 in the interface/PDR, and positions 7–10 in the molecular cloud M17-SW. The spectra were taken in the AOT 01 full scan mode at various speeds or in the AOT 06 mode with a resolving power ($\lambda/\Delta\lambda$) of 400–1600 (Table 1). The data were processed with IA^3, the SWS Interactive Analysis package using calibration files and procedures equivalent with pipeline version 10. A detailed account of the reduction can be found in Peeters et al. (2002a).

3.2. *The SpectroCam-10 Observations*

We observed IRAS 18434−0242 on UT 2001 July 6 using the SC10 MIR imaging spectrograph (Hayward et al. 1993) on the 5 m Hale telescope at Palomar Observatory. SC10 uses a 128×128 Si:As BIBIB (Back Illuminated Blocked Impurity Band) array. This instrument has both a camera and a long-slit spectrograph mode. Its pixels subtend $0''.256$ on the sky. All observations were made using a standard chop and nod sequence in beam-switching mode in order to correct for background emission from the telescope and the sky. The chopper throw is $30''$ in the north-south direction for all observations. Images are made through the filters (~ 1 μm bandpass) centered at 8.8, 10.3, and 11.7 μm with integration times of ~ 30, ~ 47, and ~ 173 s, respectively. In addition, low-resolution spectra are taken through a $1''\times16''.4$ slit that provided a spectral resolution of $R = \lambda/\Delta\lambda \sim 100$. The spectra are taken in three overlapping segments, 8.0–10.5, 9.2–12.2, and 10.4–13.4 μm, with an on-source integration time of ~ 17 minutes for slit position 1 and ~ 25 minutes for slit positions 2, 3, and 4 (Fig. 7). The seeing invoked an FWHM of $0''.7$–$1''.2$ for a standard star. No attempt was made to achieve accurate absolute astrometry at the telescope.

TABLE 1
JOURNAL OF *ISO* SWS OBSERVATIONS

Source	α (J2000.0)	δ (J2000.0)	TDT[a]	Observation[b]	References
IRAS 15567−5236	16 00 32.7	−52 44 45.3	29402535	01 (1)	
M17-1	18 20 29.0	−16 11 50.8	10201811	01 (2)	1
M17-2	18 20 27.6	−16 12 0.9	09900212	01 (2)	1
M17-3	18 20 28.2	−16 12 11.0	09901413	01 (2)	1
IRAS 18434−0242	18 46 04.1	−02 39 20.0	51300704	06	2
	18 46 04.0	−02 39 20.5	15201383	01 (2)	3
K3-50 A	20 01 45.6	+33 32 43.7	38402466	01 (4)	3

NOTE.—Units of right ascension are hours, minutes, and seconds, and units of declination are degrees, arcminutes, and arcseconds.

[a] Target Dedicated Time, uniquely identifying *ISO* observations.

[b] SWS AOT mode, with scanning speed in parentheses.

REFERENCES.—(1) Verstraete et al. 1996 for the averaged spectrum of the three positions; (2) Peeters et al. 1999; (3) Peeters et al. 2002a.

The images and spectra are processed using a library of custom routines written for the IDL environment by T. L. Hayward. The data processing includes removing bad pixels and/or frames, co-adding individual frames of an integration, dividing by flat-field images, and combining the three spectral segments into a single two-dimensional (one spectral and one spatial dimension) 8–13.2 μm spectral image of the sources along the different slits. The images are flux-calibrated against γ Aql observed at similar air mass. The mutual registration of the images is based on the assumption that the overall morphology is the same at every wavelength. In this way, the positions of the peak intensities at the three wavelengths are offset by 0.″256. The spectra are flux-calibrated against γ Aql observed through the same slit and at similar air mass as the target in combination with archival SC10 ratio spectra of the observed standard to α Lyr and the absolute α Lyr model from Cohen et al. (1992). The wavelength calibration was done using the 9.49 and 11.73 μm telluric absorption features as reference points. Some observations (slit 4) have no or low flux and hence show no or low signal-to-noise ratio (S/N) telluric absorption features. In this case, the wavelength calibration is done using the fine-structure emission lines of [S IV] at 10.5 (if present) and of [Ne II] at 12.8 μm and the PAH emission feature at 11.2 μm.

4. THE *ISO* SWS DATA

4.1. *IR Spectra*

The IR spectra of our sample sources are dominated by a strong dust continuum (Fig. 1; for IRAS 18434 and K3-50 A, see Peeters et al. [2002a]; the averaged spectrum of the three positions in M17 is shown in Verstraete et al. [1996]). On top of this continuum, there is a series of fine-structure lines and hydrogen recombination lines. In addition, the PAH emission features are present in all sources. The three compact H II regions display silicate absorption. Hence, they exhibit an IR spectrum typical for H II regions (Peeters et al. 2002a). However, they all show an extremely strong emission band in the 8–10 μm range (see Fig. 1). This feature is unlike the typical 8.6 μm PAH feature (Peeters et al. 2002b).

4.2. *Extinction Correction*

Compact H II regions are heavily embedded and suffer high visual extinctions. Since the profile of the broad emission band in the 8–10 μm range is strongly influenced by silicate absorption, we correct the spectra for extinction. The extinction at MIR wavelengths is a combination of a simple power law $A_\lambda = A_K(\lambda/2.2)^{-1.7}$ and the silicate feature. This power law appears to be independent of the line of sight. The silicate feature is derived using the results tabulated in Mathis (1990), namely, $A_{9.7}/A_K = 0.544$ for the 9.7 μm silicate feature in combination with the astronomical silicate profile of Draine (1985). The extinction due to the silicate absorption at 9.7 μm depends on the line of sight (Draine 1989), and both the shape and strength of this feature seem to vary. The silicate profile of Draine (1985) has been based on the observed Trapezium silicate profile, which is generally associated with H II regions and molecular clouds.

The A_K used to apply the extinction correction for IRAS 18434 and K3-50 is taken from Martín-Hernández et al. (2002) and equals 1.6 ± 0.2 for both sources. These authors derive A_K by comparison of the observed line strength ratios of the hydrogen recombination lines with the predictions of recombination theory assuming a nebular electron density of 1000 cm^{-3} and temperature of 7500 K. We applied the same method for IRAS 15567 and found an A_K of 1.5 ± 1.1. Similarly, we derive an A_K of 1.7 ± 0.6, 2.0 ± 0.5, and 2.7 ± 0.5 for M17-1, M17-2, and M17-3, respectively. However, we did not apply an extinction correction to these three positions within M17 because these spectra do not exhibit silicate absorption (see Fig. 1, *left panels*). An extinction correction would introduce a prominent silicate emission feature, and this seems highly contrived (intrinsic silicate emission precisely canceled by foreground absorption). In addition, there is no evidence of silicate emission in the spectra of M17.

The extinction-corrected spectra are shown in Figure 1. We emphasize that there is no evidence for a spurious 9.7 μm emission/absorption feature present in the resulting spectra owing to an overcorrection/undercorrection for extinction. Furthermore, the broad emission feature in the 8–10 μm range still remains and is thus not an artifact owing to the combination of dust continuum and silicate absorption. Hence, the reality of this feature is not in doubt.

4.3. *Band Profile*

From the wealth of IR spectra of H II regions, it is clear that in these environments the UIR bands at 3.3, 6.2, 7.7, 8.6, and 11.2 μm represent a single class of spectral features that come and go together. Since the *ISO* SWS spectra of all six positions clearly show PAH emission features (Fig. 1), the 8.6 μm PAH emission feature might be hidden in this broad emission band. In order to derive its profile, we first subtracted a local spline

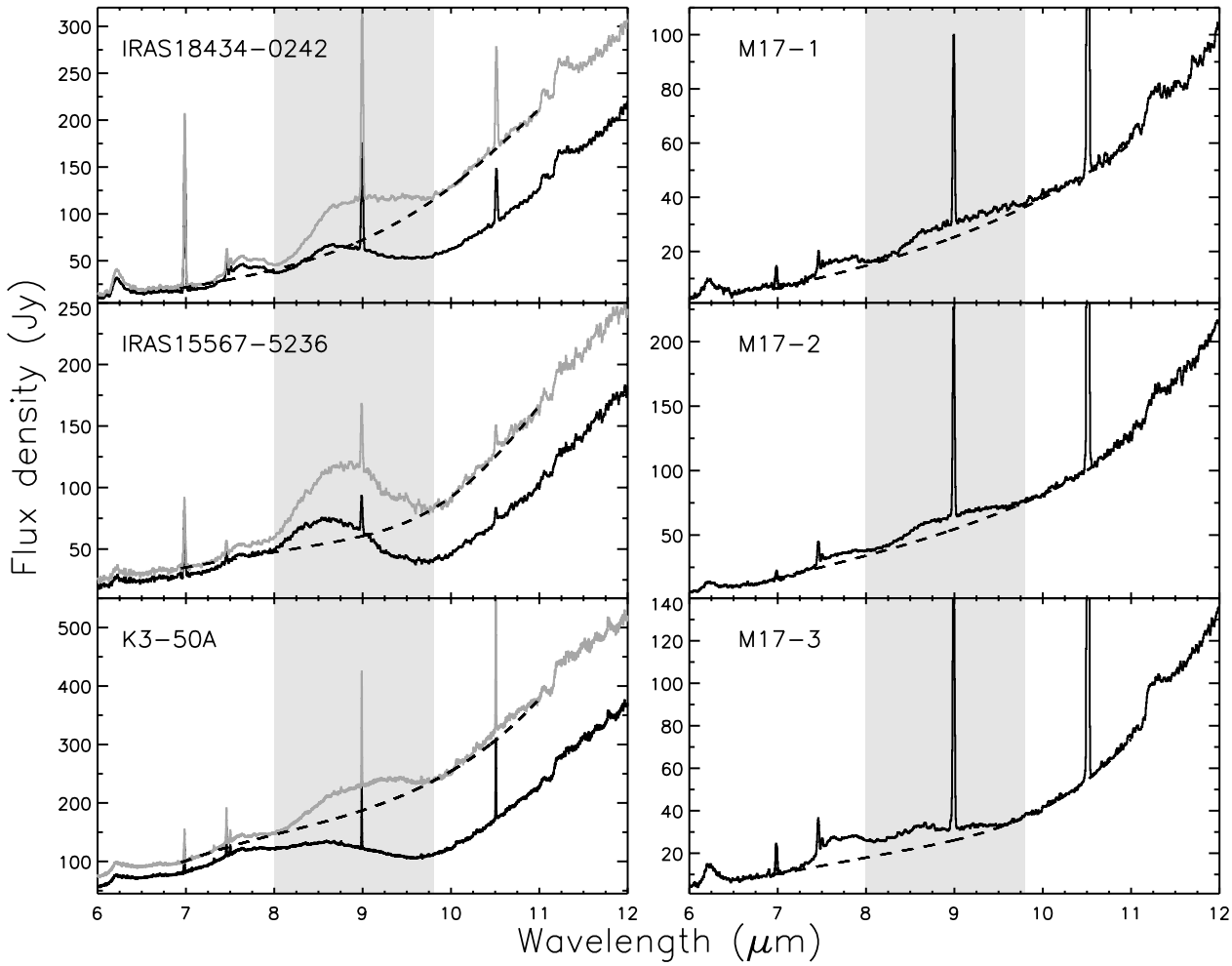

FIG. 1.—*ISO* SWS spectra of our sample (*black curve*) and the extinction-corrected spectra (*gray curve*). The adopted continua are shown by dashed curves. The gray zone indicates the region where the 8.9 μm emission is found.

continuum (Fig. 1) from the (extinction corrected) *ISO* SWS spectra (Fig. 2, *first and third columns*). The contribution of the 8.6 μm PAH band to this broad emission band is then estimated based on the following. All H II regions have the same profile for the main PAH emission features (see Peeters et al. 2002b; van Diedenhoven et al. 2004). Although the strength of the PAH bands varies from source to source, the relative strengths of the 6.2, 7.7, and 8.6 μm PAH bands are correlated with each other (Vermeij et al. 2002). In particular, the ratio of the 8.6 and 7.7 μm PAH bands equals 0.25 ± 0.03 for Galactic H II regions (Vermeij et al. 2002). Hence, by using the band profiles typical for H II regions and scaling the template to the 7.7 μm band, we can estimate the strength of the 8.6 μm band. The only unknown factor in the PAH spectrum in this wavelength region would then be the strength of the plateau, often present underneath the 7.7 and 8.6 μm PAH bands. This plateau has variable strength from source to source but is, in general, weaker (in peak intensity) than the 7.7 μm PAH band. We adopted the continuum-subtracted *ISO* SWS spectrum of IRAS 21190+5140 (Peeters et al. 1999, 2002a; TDT = 74501203) as the main PAH template (the continuum is determined in a similar way) since it suffers no extinction (Martín-Hernández et al. 2002) and has no plateau present underneath the 7.7 and 8.6 μm complex. We scaled the PAH template(s) so that the peak strength of the 7.7 μm complex, and hence the 7.6 μm subcomponent that dominates the complex in H II regions (Peeters et al. 2002b), equals that of the considered pointing (Fig. 2, *first and third columns*). Subsequently, we subtracted this scaled PAH template to derive the intrinsic profile of this emission feature (Fig. 2, *second and fourth columns*). In this way, a correction for both the 8.6 μm PAH band and the plateau emission is achieved, independent of the exact nature of their carriers.

Figures 3 and 4 illustrate the influence of variation in A_K on the derived profile of IRAS 18434. In Figure 3, A_K is varied within its derived error bars and has little influence on the peak strength and no influence on the profile itself. Figure 4 shows the derived profile with and without extinction correction. Although the strength of the feature strongly increases and the overall profile is slightly redshifted (in particular the red wing) on extinction correction, the peak position only changes slightly by at most 1 μm. The latter can be taken as a conservative uncertainty on the derived peak position of 8.9 μm, since there is no doubt about the presence of silicate absorption in this source.

To determine the influence of the presence of a plateau, we adopted the continuum-subtracted *ISO* SWS spectrum of M17-4 (ISO archive, TDT = 09900214) as a second PAH template since it exhibits a plateau, does not exhibit silicate absorption, and is the next position (after the positions discussed here) in the sequence of *ISO* SWS pointings in M17 and hence resides in the PDR. The possible presence of a plateau influences the onset of the 8.9 μm band (in the 7.7–8.3 μm range; see the panels for M17-2 and M17-3 in Fig. 2). Clearly,

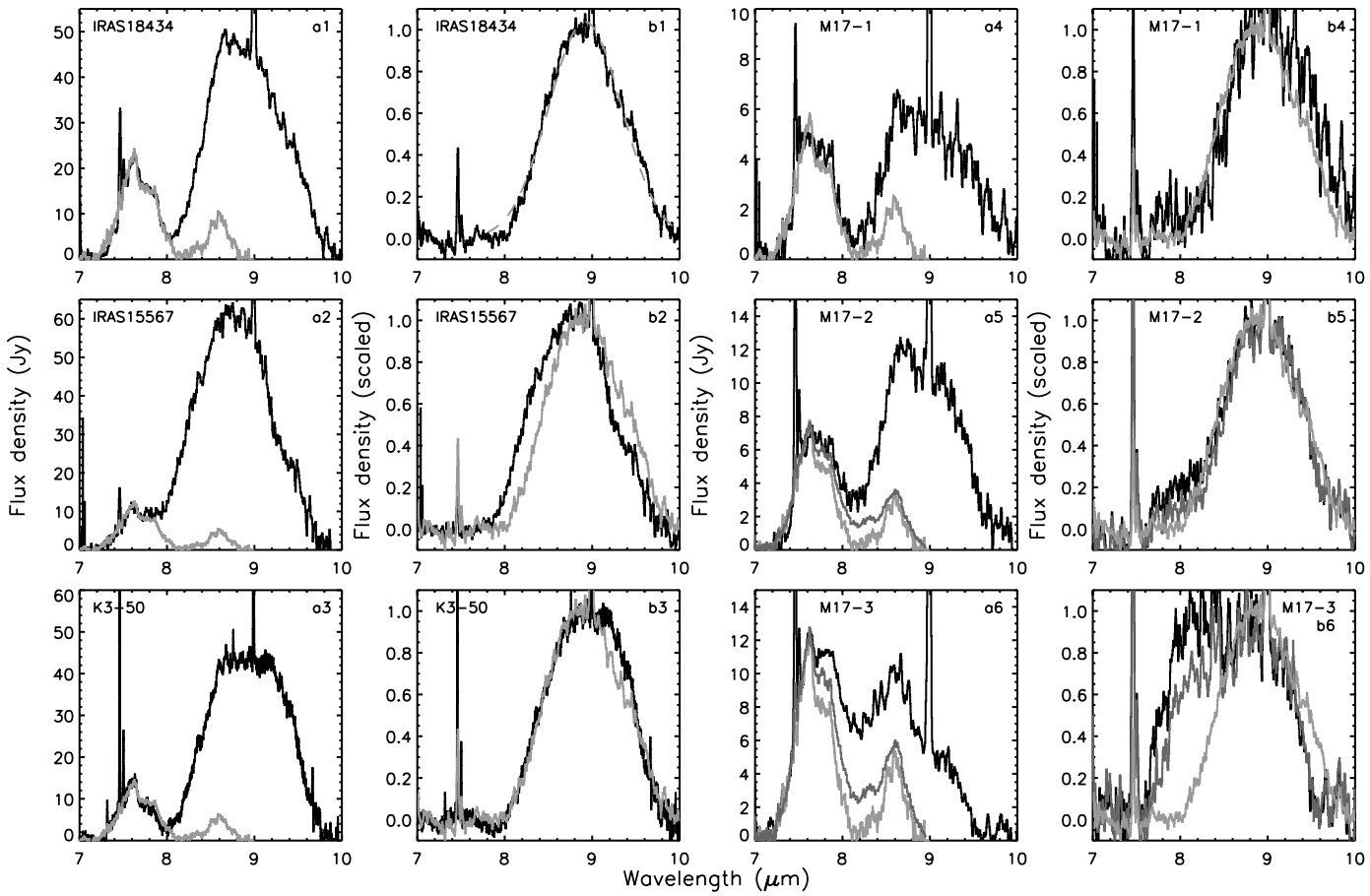

FIG. 2.—Derived profiles of the broad emission feature from 8 to 10 μm for our sample. The panels in the first and third columns show the continuum-subtracted spectra in black; the light and dark gray curves represent the PAH emission bands in the SWS spectrum of IRAS 21190+5140 and M17-4, respectively, scaled to the strength of the 7.6 μm component in each source. By subtracting these PAH templates from the continuum-subtracted spectra, we obtain the profiles of this emission feature in each source (*black and dark gray curves, respectively, second and fourth columns*). As a reference, the derived profile of IRAS 18434 is also shown in each panel in the second and fourth columns in light gray. The dashed curve in the panel for IRAS 18434 is a Gaussian fitted to the resulting profile of IRAS 18434.

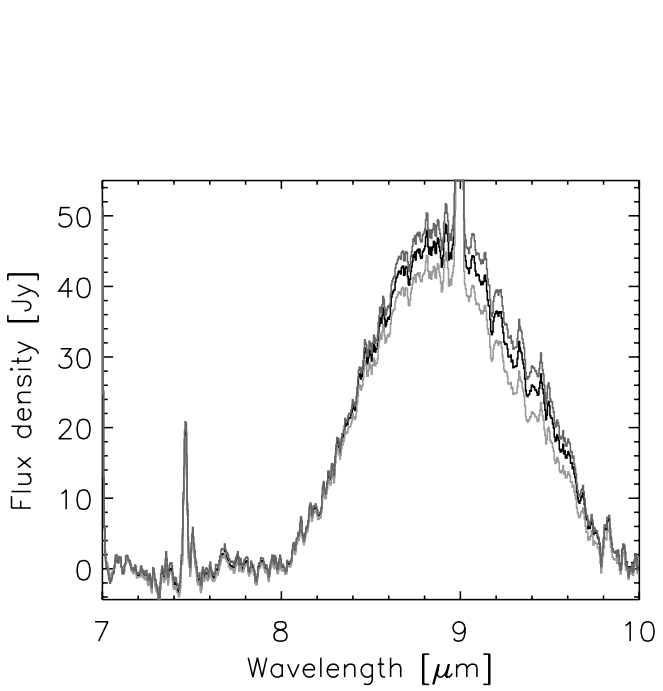

FIG. 3.—Effect of variation in A_K on the observed profiles for IRAS 18434. The black curve corresponds to $A_K = 1.6$, the dark gray curve to $A_K = 1.6 + \mathrm{error}(A_K) = 1.8$, and the light gray curve to $A_K = 1.6 - \mathrm{error}(A_K) = 1.4$.

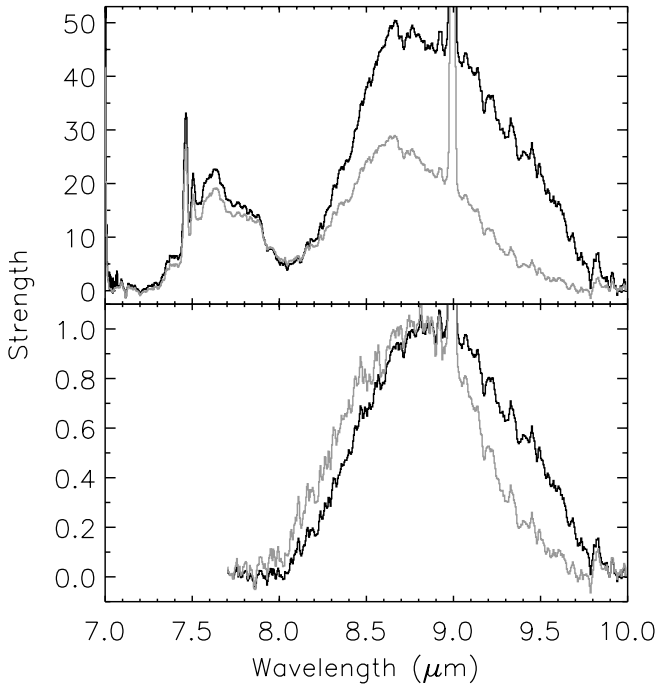

FIG. 4.—Effect of extinction correction on the derived profiles for IRAS 18434. The black and gray curves show the profile with and without extinction correction, respectively.

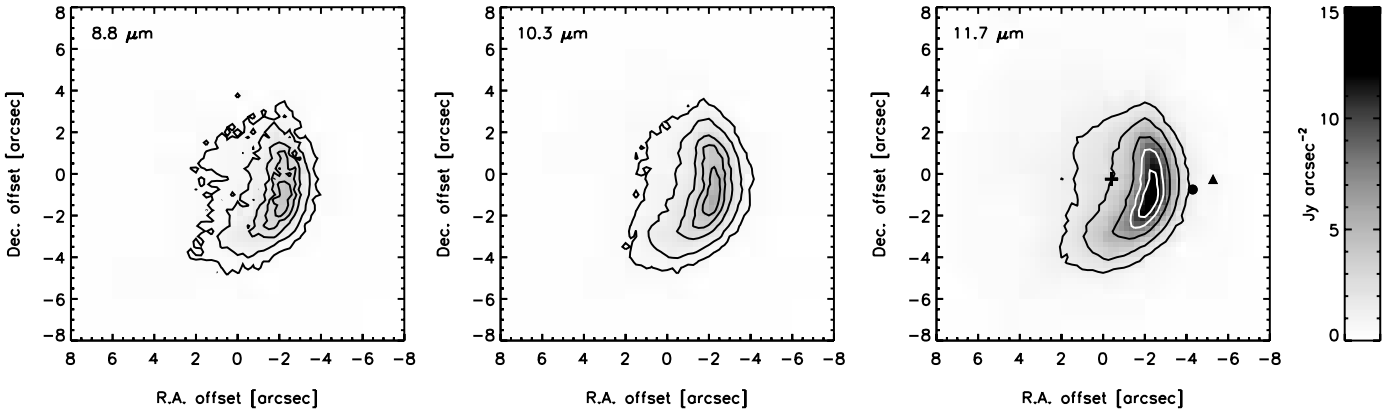

FIG. 5.—The 8.8, 10.3, and 11.7 μm images of IRAS 18434. The gray scale, indicated by the color bar, is the same for all plots. The contour levels are 0.1, 0.2, 0.4, 0.6, and 0.8 times the peak intensity for each image. This corresponds to 6, 12, 24, 37, and 49 times the rms $\sigma = 77$ mJy arcsec^{-2} for the 8.8 μm image; to 7, 14, 28, 42, and 56 times the rms $\sigma = 85$ mJy arcsec^{-2} for the 10.3 μm image; and to 11, 22, 44, 66, and 88 times the rms $\sigma = 136$ mJy arcsec^{-2} for the 11.7 μm image. The total flux is 68, 78, and 243 Jy for the 8.8, 10.3, and 11.7 μm images, respectively. The position of the ionizing star is shown by a plus sign, the NH_3 emission (Cesaroni et al. 1998) by a filled circle, and the methanol maser (Minier et al. 2000) by a filled triangle.

it has large influence on the derived profile of M17-3, but for the other sources, it is not a major issue.

The derived profiles are very broad and mostly symmetric. In addition, assuming that the extra emission in the 7.7–8.3 μm range in M17-2 is due to the plateau, four out of six positions show, within the errors, the same profile (IRAS 18434, K3-50 A, M17-1, and M17-2; Fig. 2, *second and fourth columns*). This 8.9 μm profile is well fitted by a single Gaussian with a peak position of 8.92 μm and an FWHM of 0.98 μm (panel for IRAS 18434 in Fig. 2). In contrast, the emission band in IRAS 15567 is shifted to the blue and is slightly more asymmetric. As shown in Figure 4, a lower (or no) extinction correction causes a blueshifted profile. Applying different values of A_K, we find that an increase in A_K by $\sim$1 gives the same profile as IRAS 18434. Such an increase in A_K is within the uncertainty of the derived A_K for IRAS 15567. The band in M17-3 is also shifted to the blue and has extra emission at the blue wing, at similar positions as that in M17-2. Subtracting the 8.9 μm band observed in the other sources from the observed emission in M17-3 leaves residual emission in the 7–9 μm range, which resembles the combined emission of the 7.7 μm band and the plateau of the Galactic source IRAS 16279−4757. Hence, a variable strength of this plateau can cause the observed variation in the 8.9 μm band (Fig. 2, *second and fourth columns*).

Given the uncertainty involved with the baseline correction, the extinction correction, and the removal of the 8.6 μm PAH band and plateau, the precise position of this band cannot be accurately determined. We believe that the 8.9 μm position better reflects the actual peak position of this dust feature because we have taken all of the above into account. In contrast, the 8.7 μm position derived by Verstraete et al. (1996) is obtained by only subtracting a spline function, tied to the continuum at $\sim$5.8 and $\sim$10.9 μm. Hence, these authors do not remove the certain 8.6 μm PAH and plateau contribution to this feature. Furthermore, it produces an unusually large emission plateau between 5 and 10 μm. For the remainder of this article we refer to this feature as the 8.9 μm band.

5. SPECTROCAM-10 SLIT SPECTROSCOPY OF IRAS 18434

5.1. *Infrared Images*

The three broadband images of IRAS 18434 centered at 8.8, 10.3, and 11.7 μm are shown in Figure 5. Like at other wavelengths (e.g., Wood & Churchwell 1989; Watson et al. 1997; De Buizer et al. 2002; Martín-Hernández et al. 2003), this source has a cometary appearance in the MIR at the three wavelengths (Ball et al. 1996; see Fig. 5). The filamentary-like structures to the north-northwest observed at 2 cm (Fey et al. 1995) and in the Brγ map (Watson et al. 1997) are not evident in our images. De Buizer et al. (2002) observed the HC in their high-resolution images of this source in the *N*-band filter ($\lambda_0 = 10.46$ μm, $\Delta\lambda = 5.1$ μm) with a flux density of 113 ± 17 mJy. We see no evidence for this HC in our images, as a result of the lower sensitivity of our data ($1\ \sigma = 136$ mJy) and narrower filters.

Comparison of the NIR map of Martín-Hernández et al. (2003) with the 6 cm observations of Wood & Churchwell (1989) reveals a similar morphology of the source, although the peak intensity in both maps is slightly displaced and the arcs are slightly tilted. Registration of the MIR data to the NIR map of Martín-Hernández et al. (2003) by minimizing the difference between the MIR and NIR images reveals a very good match (Fig. 6*a*). The arc and the peak intensity coincide at both wavelengths. The offset in peak intensities at NIR/MIR and radio wavelengths (Fig. 6*b*) may result from variation in density, which affects radio emission more. We note that the radio peak is located at the position where the bow shock interacts with the HC and the density is likely highest.

5.2. *The Spectra*

The different positions of the SC10 slits, typically to $\pm 0\farcs5$ accuracy, are shown on top of the 11.7 μm image in Figure 7. For further study, we have divided each slit into seven zones. We extracted SC10 spectra from each of these zones from the calibrated two-dimensional spectral image, which represents the flux densities within a zone. A few typical SC10 spectra are shown in Figure 8*a*, illustrating the spatial variety and variation. These SC10 spectra clearly show a broad emission band in the 8–10 μm range, silicate absorption at 9.7 μm, and fine-structure line emission of [Ne II] at 12.8 μm on top of a dust continuum. Fine-structure line emission of [Ar III] at 8.98 μm and the 11.2 μm PAH emission band are weakly present in some spectra. In contrast, no significant emission is seen from the fine-structure line of [S IV] at 10.5 μm in all but three individual spectra.

5.2.1. *Extinction Correction*

Watson et al. (1997) derived a map of the apparent extinction based on the 2 cm radio continuum map (Fey et al. 1995) and

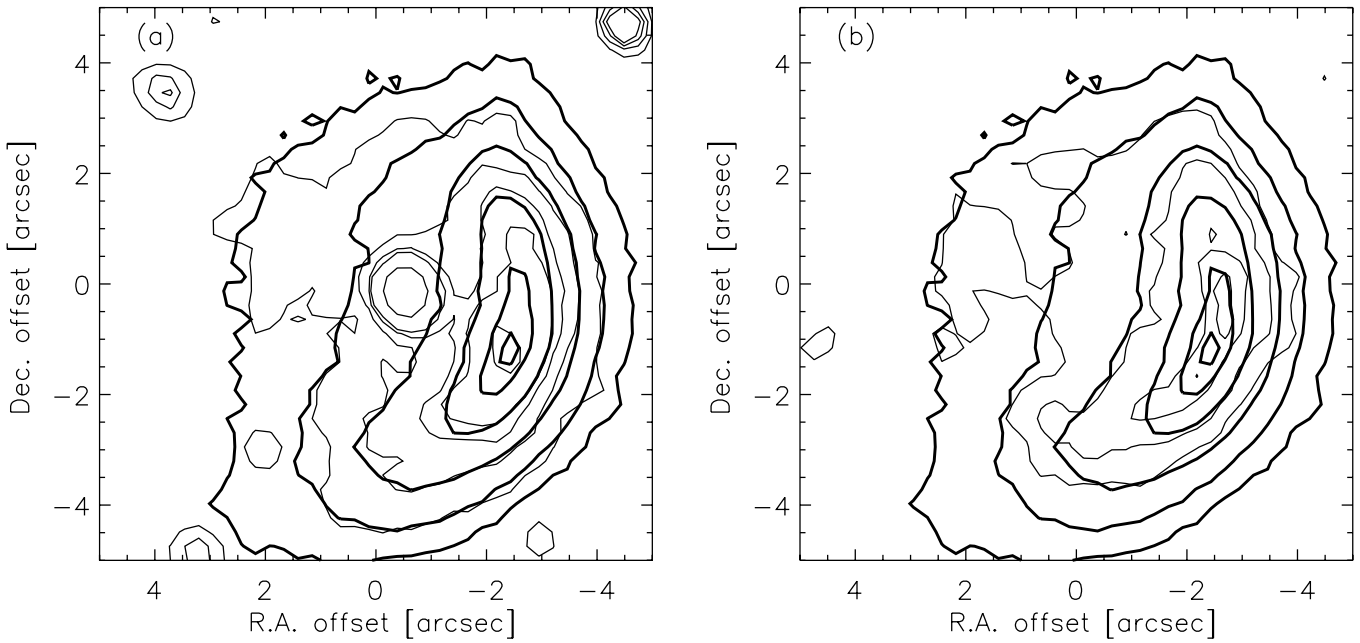

FIG. 6.—Comparison of the 11.7 μm map of IRAS 18434 (registered to the NIR map; see text; *thick contours*) with (*a*) the NIR map of Martín-Hernández et al. (2003; *thin contours*) and (*b*) the 6 cm radio map of Wood & Churchwell (1989; *thin contours*). In the NIR map, the ionizing star is present.

their 2.17 μm Brγ map. They found that the apparent extinction at Brγ varies from 1.8 to 2.6 mag, being higher in the arc and toward the end of the extension in the southeast. They give a mean value $A_K = 2.14 \pm 0.25$ and 2.2 ± 0.25 for the ionizing star. Pratap et al. (1999) estimated $A_K = 2.2 \pm 0.1$ toward the ionizing star based on the stars H–K color. Based on hydrogen recombination lines observed with *ISO* SWS, Martín-Hernández et al. (2002) reported an average extinction of $A_K = 1.6$. Martín-Hernández et al. (2002) attribute their lower extinction to the fact that the contribution of the extended envelope around the compact H II region (Kim & Koo 2001) to the SWS aperture may cause *ISO* SWS to observe a lower average hydrogen emission measure than those observed by the high $\sim 1''$ resolution observations of Watson et al. (1997) and Pratap et al. (1999).

We correct these SC10 data for extinction in the same way as the *ISO* SWS data. In Table 2 we quote for each zone the average apparent extinction obtained from this extinction map of Watson et al. (1997). For zones not covered by this map, we adopted the extinction determined by Martín-Hernández et al.

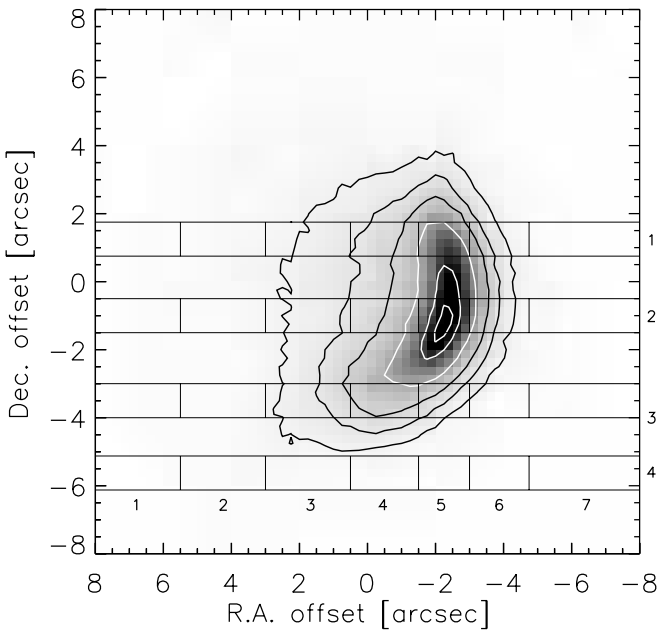

FIG. 7.—Slit positions and the zones used to extract the spectra superposed on the 11.7 μm image. Contour levels are as in Fig. 5. The slit and zone numbers are shown at, respectively, the right axis and the bottom in the plot window.

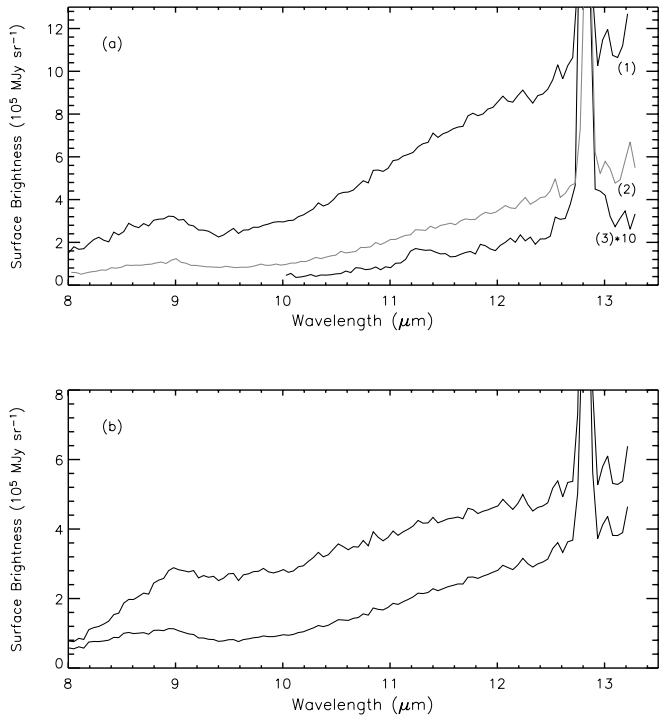

FIG. 8.—(*a*) Typical SC10 spectra of IRAS 18434 corresponding to (1) slit 2, zone 5, (2) slit 3, zone 4, and (3) slit 4, zone 1. Note the broad emission feature from 8 to 10 μm. (*b*) Observed and extinction-corrected SC10 spectra corresponding to slit 2, zone 4.

TABLE 2
THE AVERAGE APPARENT EXTINCTION IN EACH ZONE (FIG. 7)

	A_K			
ZONE	Slit 1	Slit 2	Slit 3	Slit 4
1	2.1	2.1	2.2	2.1
2	2.1	2.1	2.1	2.0
3	2.2	2.2	2.3	2.0
4	2.3	2.4	2.3	1.6*
5	2.4	2.5	2.1	1.6*
6	2.0	2.1	1.8	1.6*
7	1.6*	1.6*	1.6*	1.6*

NOTE.—Values marked with an asterisk are from Martín-Hernández et al. (2002); others are derived from Fig. 4 of Watson et al. (1997).

(2002). Figure 8*b* shows the observed and extinction-corrected SC10 spectrum of zone 4, slit 2. We emphasize that there is no evidence for a spurious 9.7 μm emission/absorption feature present in the resulting spectrum owing to an overcorrection/undercorrection for extinction. Furthermore, the broad emission feature is still present and is thus not an artifact owing to the combination of dust continuum, silicate absorption, and our limited spectral coverage.

5.2.2. *Spatial Variation*

We derive the spatial distribution of fluxes of emission features across IRAS 18434 from the extinction-corrected SC10 spectra (Fig. 9). Because of the low spectral resolution of the SC10 data, it is not possible to determine whether the spectral shape of the 8.9 μm emission feature changes with spatial position. The line fluxes are measured by subtracting a polynomial of order 2 fixed just outside the wavelength range covered by the emission line followed by fitting a Gaussian. Particular care was taken with the [Ar III] emission line because it blends with the 8.9 μm emission complex. For nondetections, we derive 3 σ upper limit fluxes, assuming a typical FWHM.

Both the [Ne II] and [Ar III] fine-structure lines clearly peak on the arc and decrease gradually with the distance from the arc. This is consistent with the [Ne II] map of Watarai et al. (1998). The [Ar III]/[Ne II] ratio is very constant and equals 0.05 ± 0.01. This contrasts with the [Ar III]/[Ne II] ratio of 0.16 ± 0.02 found in *ISO* SWS data (Peeters et al. 2002a) and of 0.13 in a detailed model of this source (Morisset et al. 2002), both after correction for an extinction of $A_K = 1.6$ (Martín-Hernández et al. 2002). Likely, this difference is due to extended low surface brightness [Ar III] emission included in the large SWS aperture but below the detection limit of our SC10 observations.

[S IV] emission is detected for only three positions, and its relation to the other lines is difficult to ascertain. For example, the [S IV] line is strongest in the northwest corner of the map (slit 1, zone 6) and has relatively low upper limits eastward in the same slit.

The dust continuum emission and the ionized gas tracers show great similarities in their overall structure, although in the arc the dust emission is somewhat more sharply peaked than

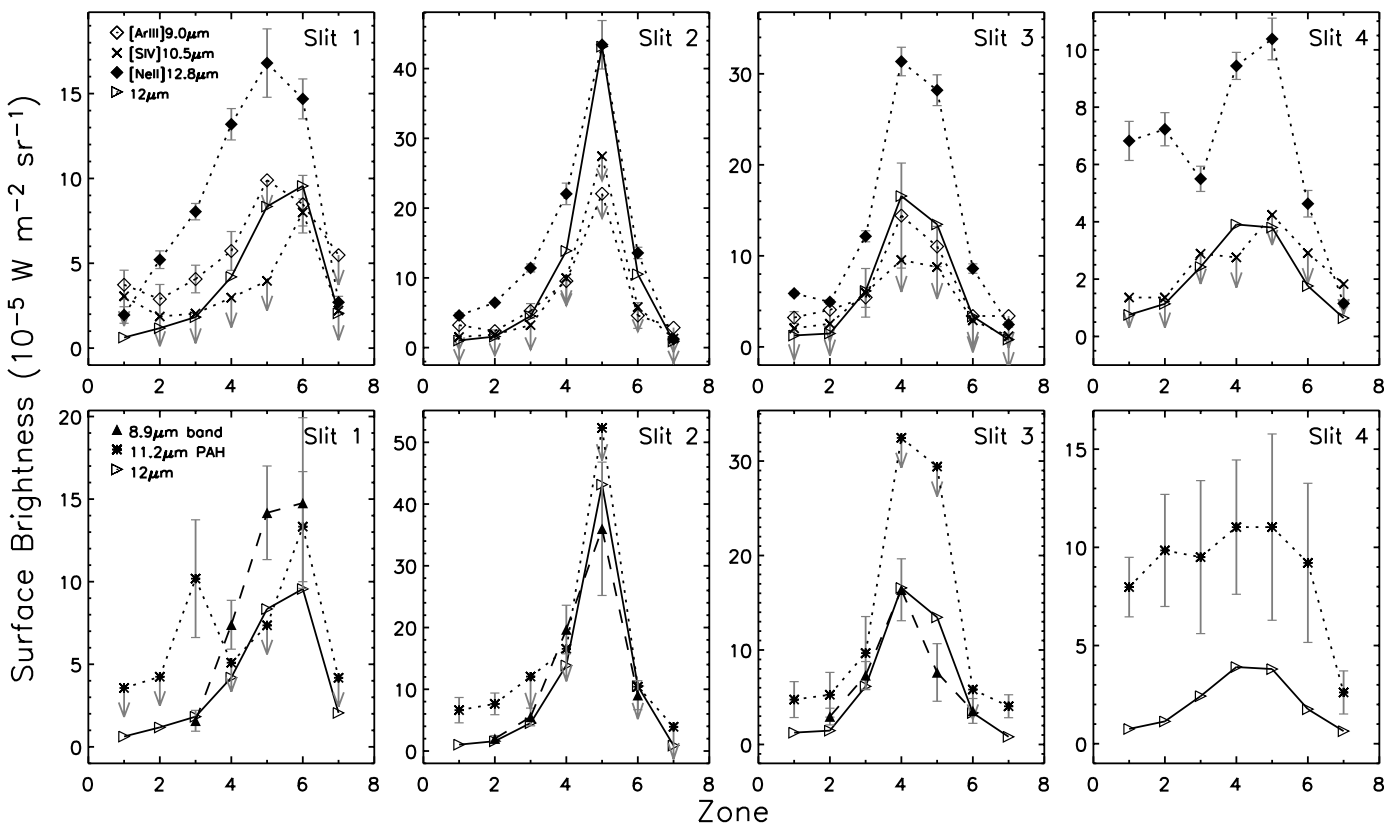

FIG. 9.—Spatial distribution of the extinction-corrected emission features across each slit. The fine-structure lines of [Ar III] 8.98 μm, [S IV] 10.51 μm, and [Ne II] 12.81 μm are shown by open diamonds, crosses, and filled diamonds, respectively, all connected by a dotted curve. The strength of the dust continuum at 12 μm given in units of 10^{-16} W m^{-2} μm^{-1} sr^{-1} is shown by open right-pointing triangles and connected by a solid curve. The broad emission feature from 8 to 9.5 μm is shown by filled upward-pointing triangles and connected by a dashed curve, and the 11.2 μm PAH emission feature is shown by asterisks and connected by a dotted curve. Furthermore, the [Ne II] fluxes are divided by 10, the strength of the dust continuum by 70, and the flux of the broad emission feature from 8 to 9.5 μm by 20. Note that for slit 4, the short-wavelength region (<10 μm) has insufficient S/N and is not shown here.

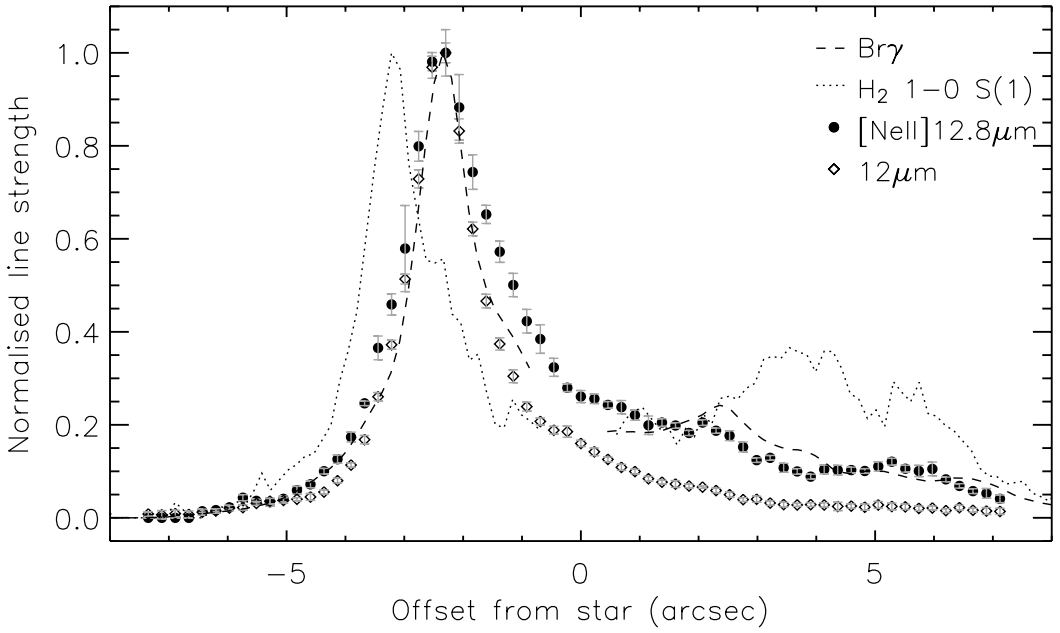

FIG. 10.—Spatial variation of the [Ne II] 12.8 μm fine-structure line and the strength of the 12 μm continuum across slit 2 projected on the symmetry axis of IRAS 18434 (63°.8 with respect to the north-south axis) compared to the Brγ and H_2 1–0 $S(1)$ of Martín-Hernández et al. (2003). The origin corresponds to the position of the ionizing star. No extinction correction is applied.

the [Ne II] line (Figs. 9 and 10). In contrast, the 11.2 μm PAH emission feature, detected in about half of the obtained spectra, is very differently distributed. The emission is strongest off-source: all zones of slit 4 exhibit 11.2 μm emission, while for slits 2 and 3 emission is only detected in the easternmost/westernmost zones. In slit 1 PAH emission is detected closest to the arc (zones 3 and 6). Finally, the 8.9 μm emission feature is present in all but the outer zones in the three slits located on the source; thus, its spatial distribution resembles that of the dust continuum and the [Ne II] fine-structure line but differs greatly from that of the 11.2 μm PAH emission.

To gain additional insight into the structure of the IRAS 18434 nebula, we compare our 10 μm data with near-IR tracers. High-resolution, long-slit *K*-band spectra along the east-west symmetry axis of the source show that the He I and Brγ lines have distinct distributions compared to H_2 (Martín-Hernández et al. 2003; Fig. 10). H_2 peaks 0".93 ahead of the Brγ maximum and exhibits a different structure in the tail of IRAS 18434. Note that this is not obvious from Figure 6. Indeed, although taken through the narrowband filter at 2.13 μm, the NIR map is dominated by the continuum and not the H_2 emission (Martín-Hernández et al. 2003, Figs. 1 and 2). Our SC10 slit 2 lies along the same symmetry axis, and the large strength of the [Ne II] 12.8 and 12 μm dust continuum emission allows us to construct similar high-resolution spatial profiles. Both [Ne II] and the dust emission peak at the same location as the Brγ emission (Fig. 10). Furthermore, the [Ne II] emission shows a second peak at a similar location (~2".3) as the Brγ emission although a similar third bump in the [Ne II] (~5".3) is absent in Brγ. This second bump seems also to be present in the dust emission, although much weaker. The strong secondary peak in the H_2 emission at 3".8 is absent in both [Ne II] and the dust continuum, although it roughly coincides with the position where we detect PAH emission.

Summarizing, IRAS 18434 exhibits the following layered structure. Of all tracers, the 12 μm dust continuum emission is most strongly centrally peaked. The 8.9 μm emission feature shows a similar distribution but differs in detail. The "nebular" lines [Ar III], [Ne II], and Brγ all are somewhat more extended. The molecular emission, from H_2 and PAHs (11.2 μm), is least centrally concentrated.

6. M17

Verstraete et al. (1996; see their Fig. 3) detected an 8.7 μm band in M17. This band corresponds to the 8.9 μm band as discussed in § 4. Although these authors derived the band in a different way (§ 4), the spatial variation in the intensity is similar to what we derived for the 8.9 μm band. These authors studied the spatial variation of the different dust components and conclude that (1) all PAH features peak at the interface (positions 4–5); (2) conversely, the 16 μm continuum decreases monotonously away from position 2; and (3) in the H II region, the 8.9 μm band intensity follows the 16 μm continuum. We also checked the intensity ratios of [Ne III]/[Ne II] (15.5/12.8 μm) and [Ar III]/[Ar II] (9.0/7.0 μm), both indicators of the hardness of the radiation field. These ratios decrease monotonously away from position 2, as do the 16 μm continuum and the 8.9 μm band. Hence, the 8.9 μm band is strongest where the radiation field is the hardest.

7. DISCUSSION

The 8.9 μm emission feature is a "new" feature, not a peculiarity of the possible variations in the 8.6 μm PAH band (Peeters et al. 2002b) for the following reasons. First, the spatial distribution of the 8.9 μm emission feature is distinct from that of other PAH features. Second, the observed intensity of this 8.9 μm band strongly exceeds the expected 8.6 μm band intensity based on the 6.2 and 7.7 μm PAH features. Indeed, Vermeij et al. (2002) show that the strengths of the 6.2, 7.7, and 8.6 μm PAH bands correlate with each other. Third, while the profile of the 8.9 μm band is somewhat uncertain, it is clearly distinct from that of the 8.6 μm PAH band (Peeters et al. 2002b) as it is much broader and peaks at higher wavelengths. Hence, we can conclude that the observed 8.9 μm emission band is not the traditional 8.6 μm PAH band.

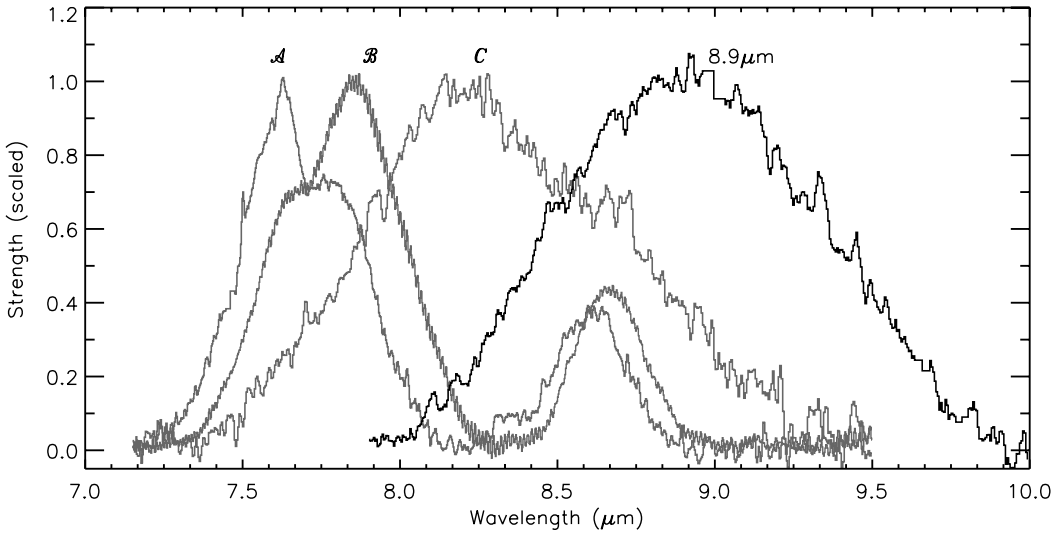

FIG. 11.—Overview of the PAH emission band classes as classified by Peeters et al. (2002b). The spectra are normalized so that the peak intensity equals 1. Clearly, the emission band at 8.9 μm does not fall in any of the classes ($\mathcal{A}$, $\mathcal{B}$, or $\mathcal{C}$).

The 8.9 μm profile is well fitted by a single Gaussian with a peak position of 8.92 μm and an FWHM of 0.98 μm (Fig. 2). Four of the six positions show exactly the same profile. Two other positions show excess emission at the blue wavelength sides, which may, however, reflect an improper correction for the PAH plateau underneath the 7.7 and 8.6 μm complex and/or extinction. We did not find a source-to-source relation between the strength of the 8.9 μm band and any PAH emission feature. Keep in mind that this is based on a small source sample of one highly excited extended H II region (M17) and three (ultra)compact H II regions.

7.1. *Spatial Distribution*

The large difference in the distribution of the PAHs, located in the PDR, and the 8.9 μm band indicates that the 8.9 μm band resides within the H II region.

Comparison of the spatial distribution of the Brγ, H_2, [Ne II], and dust continuum emission in IRAS 18434 might reveal the location of the dust and the carrier of the 8.9 μm band (in the H II regions or in the PDR). Indeed, since the observed H_2 emission likely arises from the PDR (Martín-Hernández et al. 2003), the separation between the H_2 and the ionized gas (Fig. 10) measures directly the far-ultraviolet penetration size scale (Tielens & Hollenbach 1985). With the observed scale size of the H_2 emission and assuming that there is a ΔA_V of $\simeq$0.5 mag between the ionization front and the dust emission peak in the PDR, a separation of 0.″23 between the peaks of the emission from dust located in the PDR and the tracers of the H II region is obtained. However, our study has a spatial resolution of 0.″256 pixel^{-1} and a seeing of 0.″6; hence, a separation of 0.″23 is not resolved. Therefore, the fact that the dust emission and the 8.9 μm band show a similar spatial distribution compared to the [Ne II] emission does not necessarily imply that the dust and the carrier of the 8.9 μm band are colocated with the ionized gas. However, as mentioned above, the large difference in the distribution of the PAHs and the 8.9 μm band indicates that the 8.9 μm band resides within the H II region. This is confirmed by the extended H II region M17 where both the dust (dominating the emission at MIR wavelengths) and the 8.9 μm band carrier reside well inside the H II region. Moreover, they are strongest at positions where the radiation field is hardest (as traced by the fine-structure lines; see § 6), and the 8.9 μm band is not seen in the PDR or the molecular cloud.

7.2. *The Identification*

The 8.9 μm band follows the dust emission rather than the PAH emission (see §§ 5.2 and 6) and resides within the H II region. Hence, its carrier should be much less susceptible to destruction than the PAHs. This would indicate a larger size for the 8.9 μm carrier.

The presence of this band in sources otherwise characterized by PAH emission features may be taken to suggest a similar carrier. The spectral characteristics of the emission features in the 6–9 μm region are known to be highly variable (Peeters et al. 2002b). Comparison of the profile of the 8.9 μm feature with those of other sources reveals that this feature is clearly distinct and unique (Fig. 11). Indeed, the peak position is at longer wavelengths (by >0.7 μm) compared to any PAH-related emission profile found so far. Furthermore, only the profile of class $\mathcal{C}$ has a comparable FWHM (Peeters et al. 2002b). On the basis of this comparison, it is suggestive that the shift to longer wavelengths of the peak position seems connected to an increase in the width and a more "amorphous" feature. *Considering for the moment* a PAH-related carrier, the shift and broadening of profile $\mathcal{C}$ of the "7.7 μm " feature, as well as that of the 8.9 μm feature, may reflect an increased modification of the carrier. This is possibly due to an increased clustering into larger and larger units. Given that the 8.9 μm feature has a different spatial distribution than the PAH features in IRAS 18434 and M17, whatever process is modifying the PAHs has to be active within this source. Since the 8.9 μm feature is more closely connected to the H II region, density variations may be at the bottom of the spectral variation.

Arguments in favor of a PAH-related carrier are the presence of the 8.9 μm feature in "PAH" sources that do not show any other discernible dust feature (except silicate in absorption) and possibly the spectral sequence illustrated in Figure 11. Arguments against a connection of the 8.9 μm feature with PAHs or PAH-related materials are that (1) while the PAH features dominate the MIR of many objects, in a very large sample, these are the only sources with such a remarkable feature (e.g.,

Peeters et al. 2002b); and (2) the different spatial distribution of the PAH features and the 8.9 μm feature. A further argument against a PAH-related origin is that neither the laboratory PAH spectra currently available nor any known hydrogenated amorphous carbon (HAC) can reproduce this feature.

The different spatial distribution compared to the PAH features and the large FWHM of the 8.9 μm feature suggest a grainlike carrier. Various carbonaceous materials show an emission near 8 μm, including HAC, quenched carbon composites (QCCs), coal, and partially hydrogenated C_{60} (Mortera & Low 1983; Sakata et al. 1984; Colangeli et al. 1995; Guillois et al. 1996; Scott et al. 1997; Schnaiter et al. 1999; Stoldt et al. 2001). However, the profiles in these solid-state materials peak close to 8 μm and are much broader than the 8.9 μm feature. Therefore, these materials cannot be the carrier of this 8.9 μm feature. Various O-rich materials also show emission in this wavelength region (Speck 1998; Molster et al. 2002). The most likely candidate is silica (Speck 1998; Speck et al. 2000; Fabian et al. 2000; SiO_2). However, the 9.2 μm silica profile is clearly asymmetric and peaks at slightly longer wavelengths compared to the 8.9 μm feature.

In conclusion, better understanding of the carrier of the 8.9 μm feature awaits further laboratory and astronomical studies. A forthcoming paper addresses the excitation conditions and evolution of the carrier of the 8.9 μm emission feature.

8. SUMMARY

In this paper the *ISO* SWS high-resolution spectra of three compact H II regions (IRAS 15567−5236, IRAS 18434−0242, K3-50 A) and three positions within the H II region M17 are presented along with MIR images and long-slit 8–13 μm spectra of IRAS 18434−0242 obtained with SpectroCam-10 at Palomar Observatory. Two of these sources have been known to exhibit peculiar strong emission in the 8–9 μm range, clearly distinct from the classical 8.6 μm PAH band (Roelfsema et al. 1996; Verstraete et al. 1996; Peeters et al. 2002b). Here we double the number of sources exhibiting this peculiar emission and carefully derive the feature's profile. Four of the six positions show exactly the same profile, being clearly symmetric, peaking at $\sim$8.9 μm, and having an FWHM of $\sim$1 μm. Two other positions show excess emission at the blue wavelength sides compared to this profile. This difference may, however, reflect an improper correction for the PAH plateau underneath the 7.7 and 8.6 μm complex, which is variable in strength from source to source.

We discuss the spatial distribution of the emission features in M17 and IRAS 18434−0242. The spatial distribution of the 8.9 μm feature is clearly different from that of the main PAH bands. However, it resembles well that of the ionized gas and especially that of the dust continuum at 15 μm. The spatial information of IRAS 18434−0242 is insufficient to determine whether the 8.9 μm feature resides inside the H II region or in the PDR. However, in M17, the carrier of this feature is located inside the H II region. Moreover, this band is not detected in the PDR and the molecular cloud of M17.

The presence of the carrier in the H II regions indicates that it is less susceptible to destruction than the PAHs. Previous studies have shown that the 7.7 μm UIR emission feature can shift to 8.22 μm in some sources (Peeters et al. 2002b), and this spectral variation has been attributed to a growth in size of the emission carrier. Possibly, this 8.9 μm band is just an extreme example of such a shift and its carrier is closely related to the carriers of the UIR bands. However, none of the currently available spectra of different types of carbonaceous, PAH-like dust materials can reproduce this feature, nor do various O-rich materials. Hence, a clear identification of this feature awaits further laboratory and astronomical studies.

We thank the staff of Palomar Observatory for assistance with the observations. We are grateful to A. Bik, E. Churchwell, L. Martín-Hernández, and A. Watson for providing data of IRAS 18434. E. P. thanks N. L. Martín-Hernández, C. Alvarez, and H. Spoon for useful discussions. This paper is based on observations made with *ISO*, an ESA project with instruments funded by ESA member states (especially the PI countries: France, Germany, the Netherlands, and the United Kingdom) and with the participation of ISAS and NASA. E. P. acknowledges the support of an NWO program subsidy (grant 783-70-000) and the National Research Council.

REFERENCES

Allamandola, L. J., Tielens, A. G. G. M., & Barker, J. R. 1985, ApJ, 290, L25
———. 1989, ApJS, 71, 733
Alvarez, C., Feldt, M., Henning, T., Puga, E., & Brandner, W. 2004, ApJS, 155, 123
Araya, E., Hofner, P., Churchwell, E., & Kurtz, S. 2002, ApJS, 138, 63
Ball, R., Meixner, M. M., Keto, E., Arens, J. F., & Jernigan, J. G. 1996, AJ, 112, 1645
Barlow, M. J., & Silk, J. 1977, ApJ, 211, L83
Bregman, J. 1989, in IAU Symp. 135, Interstellar Dust, ed. L. J. Allamandola & A. G. G. M. Tielens (Dordrecht: Kluwer), 109
Bregman, J., & Temi, P. 2005, ApJ, in press
Bronfman, L., Nyman, L., & May, J. 1996, A&AS, 115, 81
Burton, M. G., Hollenbach, D. J., & Tielens, A. G. G. M. 1990, ApJ, 365, 620
Burton, M. G., Londish, D., & Brand, P. W. J. L. 2002, MNRAS, 333, 721
Cesaroni, R., Churchwell, E., Hofner, P., Walmsley, C. M., & Kurtz, S. 1994, A&A, 288, 903
Cesaroni, R., Hofner, P., Walmsley, C. M., & Churchwell, E. 1998, A&A, 331, 709
Cesarsky, D., et al. 1996, A&A, 315, L309
Chini, R., Elsaesser, H., & Neckel, T. 1980, A&A, 91, 186
Churchwell, E., Walmsley, C. M., & Cesaroni, R. 1990, A&AS, 83, 119
Churchwell, E., Walmsley, C. M., & Wood, D. O. S. 1992, A&A, 253, 541
Cohen, M., Walker, R. G., Barlow, M. J., & Deacon, J. R. 1992, AJ, 104, 1650
Colangeli, L., Mennella, V., Palumbo, P., Rotundi, A., & Bussoletti, E. 1995, A&AS, 113, 561
De Buizer, J. M., Watson, A. M., Radomski, J. T., Piña, R. K., & Telesco, C. M. 2002, ApJ, 564, L101
de Graauw, T., et al. 1996, A&A, 315, L49
de Pree, C. G., Goss, W. M., Palmer, P., & Rubin, R. H. 1994, ApJ, 428, 670
Draine, B. T. 1985, ApJS, 57, 587
———. 1989, in Infrared Spectroscopy in Astronomy, ed. B. H. Kaldeich (ESA SP-290; Paris: ESA), 93
Draine, B. T., & Salpeter, E. E. 1979a, ApJ, 231, 77
———. 1979b, ApJ, 231, 438
Ellingsen, S. P., et al. 1996, MNRAS, 280, 378
Fabian, D., Jäger, C., Henning, T., Dorschner, J., & Mutschke, H. 2000, A&A, 364, 282
Felli, M., Churchwell, E., & Massi, M. 1984, A&A, 136, 53
Fey, A. L., Gaume, R. A., Claussen, M. J., & Vrba, F. J. 1995, ApJ, 453, 308
Gatley, I., Becklin, E. E., Sellgren, K., & Werner, M. W. 1979, ApJ, 233, 575
Geballe, T. R., Tielens, A. G. G. M., Allamandola, L. J., Moorhouse, A., & Brand, P. W. J. L. 1989, ApJ, 341, 278
Gibb, A. G., Wyrowski, F., & Mundy, L. G. 2004, ApJ, 616, 301
Guillois, O., Nenner, I., Papoular, R., & Reynaud, C. 1996, ApJ, 464, 810
Hanson, M. M., Howarth, I. D., & Conti, P. S. 1997, ApJ, 489, 698
Hatchell, J., Thompson, M. A., Millar, T. J., & MacDonald, G. H. 1998, A&AS, 133, 29
Hayward, T. L., Miles, J. E., Houck, J. R., Gull, G. E., & Schoenwald, J. 1993, Proc. SPIE, 1946, 334
Hofmann, K. H., Balega, Y., Preibisch, T., & Weigelt, G. 2004, A&A, 417, 981
Hofner, P., & Churchwell, E. 1996, A&AS, 120, 283

Hony, S., et al. 2001, A&A, 370, 1030
Howard, E. M., Pipher, J. L., Forrest, W. J., & de Pree, C. G. 1996, ApJ, 460, 744
Icke, V., Gatley, I., & Israel, F. P. 1980, ApJ, 236, 808
Jiang, Z., et al. 2002, ApJ, 577, 245
Joblin, C., Tielens, A. G. G. M., Geballe, T. R., & Wooden, D. H. 1996, ApJ, 460, L119
Kahn, F. D. 1974, A&A, 37, 149
Kaper, L., Bik, A., Hanson, M., & Comerón, F. 2002a, in ASP Conf. Ser. 267, Hot Star Workshop III: The Earliest Phases of Massive Star Birth, ed. P. Crowther (San Francisco: ASP), 95
———. 2002b, in The Origins of Stars and Planets: The VLT View, ed. J. Alves & M. McCaughrean (Garching: ESO), 291
Kessler, M. F., et al. 1996, A&A, 315, L27
Kim, K., & Koo, B. 2001, ApJ, 549, 979
Kurtz, S., Churchwell, E., & Wood, D. O. S. 1994, ApJS, 91, 659
Lada, C. J. 1976, ApJS, 32, 603
Larson, R. B., & Starrfield, S. 1971, A&A, 13, 190
Léger, A., & Puget, J. L. 1984, A&A, 137, L5
Linke, R. A., & Goldsmith, P. F. 1980, ApJ, 235, 437
Lobert, W., & Goss, W. M. 1978, MNRAS, 183, 119
Lumsden, S. L., & Hoare, M. G. 1996, ApJ, 464, 272
Maillard, J. P., Joblin, C., Mitchell, G. F., Vauglin, I., & Cox, P. 1999, in The Universe as Seen by *ISO*, ed. P. Cox & M. F. Kessler (ESA SP-427; Noordwijk: ESA), 707
Martín-Hernández, N. L., Bik, A., Kaper, L., & Tielens, A. G. G. M. 2003, A&A, 405, 175
Martín-Hernández, N. L., et al. 2002, A&A, 381, 606
Mathis, J. S. 1970, ApJ, 159, 263
———. 1990, ARA&A, 28, 37
Maxia, C., Testi, L., Cesaroni, R., & Walmsley, C. M. 2001, A&A, 371, 287
Meixner, M., Haas, M. R., Tielens, A. G. G. M., Erickson, E. F., & Werner, M. 1992, ApJ, 390, 499
Minier, V., & Booth, R. S. 2002, A&A, 387, 179
Minier, V., Booth, R. S., & Conway, J. E. 2000, A&A, 362, 1093
Miyata, T., et al. 2004, A&A, 415, 179
Molster, F. J., Waters, L. B. F. M., & Tielens, A. G. G. M. 2002, A&A, 382, 222
Morisset, C., et al. 2002, A&A, 386, 558
Mortera, C., & Low, M. J. D. 1983, Carbon, 21, 283
Ogura, K., & Ishida, K. 1976, PASJ, 28, 35
Okamoto, Y. K., et al. 2003, ApJ, 584, 368
Peeters, E., Allamandola, L. J., Hudgins, D. M., Hony, S., & Tielens, A. G. G. M. 2004a, in ASP Conf. Ser. 309, Astrophysics of Dust, ed. A. N. Witt, G. C. Clayton, & B. T. Draine (San Francisco: ASP), 141
Peeters, E., Spoon, H. W. W., & Tielens, A. G. G. M. 2004b, ApJ, 613, 986
Peeters, E., Tielens, A. G. G. M., Roelfsema, P. R., & Cox, P. 1999, in The Universe as Seen by *ISO*, ed. P. Cox & M. F. Kessler (ESA SP-427; Noordwijk: ESA), 739
Peeters, E., et al. 2002a, A&A, 381, 571
———. 2002b, A&A, 390, 1089
Pestalozzi, M., Humphreys, E. M. L., & Booth, R. S. 2002, A&A, 384, L15
Phillips, J. P., & Mampaso, A. 1991, A&AS, 88, 189
Pratap, P., Megeath, S. T., & Bergin, E. A. 1999, ApJ, 517, 799
Pratap, P., Menten, K. M., & Snyder, L. E. 1994, ApJ, 430, L129
Puget, J. L., & Léger, A. 1989, ARA&A, 27, 161
Roelfsema, P. R., Goss, W. M., & Geballe, T. R. 1988, A&A, 207, 132
Roelfsema, P. R., et al. 1996, A&A, 315, L289
Rubin, R. H., & Turner, B. E. 1969, ApJ, 157, L41
Sakata, A., Wada, S., Tanabe, T., & Onaka, T. 1984, ApJ, 287, L51
Schnaiter, M., et al. 1999, ApJ, 519, 687
Schraml, J., & Mezger, P. G. 1969, ApJ, 156, 269
Scott, A. D., Duley, W. W., & Jahani, H. R. 1997, ApJ, 490, L175
Speck, A. K. 1998, Ph.D. thesis, Univ. College London
Speck, A. K., Barlow, M. J., Sylvester, R. J., & Hofmeister, A. M. 2000, A&AS, 146, 437
Stoldt, C. R., Maboudian, R., & Carraro, C. 2001, ApJ, 548, L225
Stutzki, J., & Guesten, R. 1990, ApJ, 356, 513
Stutzki, J., et al. 1988, ApJ, 332, 379
Tielens, A. G. G. M., & Hollenbach, D. 1985, ApJ, 291, 722
Turner, B. E., & Matthews, H. E. 1984, ApJ, 277, 164
van Diedenhoven, B., et al. 2004, ApJ, 611, 928
Van Kerckhoven, C., et al. 2000, A&A, 357, 1013
Vermeij, R., Peeters, E., Tielens, A. G. G. M., & van der Hulst, J. M. 2002, A&A, 382, 1042
Verstraete, L., et al. 1996, A&A, 315, L337
Walsh, A. J., Burton, M. G., Hyland, A. R., & Robinson, G. 1998, MNRAS, 301, 640
Walsh, A. J., Hyland, A. R., Robinson, G., & Burton, M. G. 1997, MNRAS, 291, 261
Watarai, H., Matsuhara, H., Takahashi, H., & Matsumoto, T. 1998, ApJ, 507, 263
Watson, A. M., Coil, A. L., Shepherd, D. S., Hofner, P., & Churchwell, E. 1997, ApJ, 487, 818
Watson, A. M., & Hanson, M. M. 1997, ApJ, 490, L165
Wink, J. E., Wilson, T. L., & Bieging, J. H. 1983, A&A, 127, 211
Wolfire, M. G., & Cassinelli, J. P. 1987, ApJ, 319, 850
Wood, D. O. S., & Churchwell, E. 1989, ApJS, 69, 831
Wynn-Williams, C. G., Matthews, K., Werner, M. W., Becklin, E. E., & Neugebauer, G. 1977, MNRAS, 179, 255
Yorke, H. W. 1986, ARA&A, 24, 49